\



Solving the time-dependent Schrödinger equation by combining smooth exterior complex scaling and Arnoldi propagator

Shun Wang(王顺) and Wei-Chao Jiang(姜维超)
Citation: Chin. Phys. B, 2022, 31 (**1**): 013201. DOI: 10.1088/1674-1056/ac11d6
Journal homepage: http://cpb.iphy.ac.cn; http://iopscience.iop.org/cpb

What follows is a list of articles you may be interested in

Influence of Coulomb force between two electrons on double ionization of He-like atoms

Peipei Liu(刘培培), Yongfang Li(李永芳), and Jingtao Zhang(张敬涛)
Chin. Phys. B, 2022, 31 (**1**): 013202. DOI: 10.1088/1674-1056/ac0cdf

Taking snapshots of a moving electron wave packet in molecules using photoelectron holography in strong-field tunneling ionization

Mingrui He(何明睿), Yang Fan(樊洋), Yueming Zhou(周月明), and Peixiang Lu(陆培祥)
Chin. Phys. B, 2021, 30 (**12**): 123202. DOI: 10.1088/1674-1056/abf7a7

Molecular photoelectron momentum and angular distributions of N_2 molecules by ultrashort attosecond laser pulses

Si-Qi Zhang(张思琪), Qi Zhen(甄琪), Zhi-Jie Yang(杨志杰), Jun Zhang(张军), Ai-Hua Liu(刘爱华), Kai-Jun Yuan(元凯军), Xue-Shen Liu(刘学深), and Jing Guo(郭静)
Chin. Phys. B, 2021, 30 (**4**): 043201. DOI: 10.1088/1674-1056/abca22

Ultrafast photoionization of ions and molecules by orthogonally polarized intense laser pulses: Effects of the time delay

Si-Qi Zhang(张思琪), Zhi-Jie Yang(杨志杰), Zhi-Xian Lei(雷志仙), Wei Feng(冯伟), Sheng-Peng Zhou(周胜鹏), Kai-Jun Yuan(元凯军), Xue-Shen Liu(刘学深), and Jing Guo(郭静)
Chin. Phys. B, 2021, 30 (**1**): 013201. DOI: 10.1088/1674-1056/abb30c

Photoelectron imaging on vibrational excitation and Rydberg intermediate states in multi-photon ionization process of NH_3 molecule

Ya-Nan Sun(孙亚楠), Yan-Hui Wang(王艳辉), Le-Le Song(宋乐乐), Hai-Bin Du(杜海滨), Xiao-Chun Wang(王晓春), Lan-Lai He(赫兰海), Si-Zuo Luo(罗嗣佐), Qin Yang(杨钦), Jing Leng(冷静), Fu-Chun Liu(刘福春)
Chin. Phys. B, 2020, 29 (**9**): 093201. DOI: 10.1088/1674-1056/ab9431

Solving the time-dependent Schrödinger equation by combining smooth exterior complex scaling and Arnoldi propagator

Shun Wang(王顺) and Wei-Chao Jiang(姜维超)†

College of Physics and Optoelectronic Engineering, Shenzhen University, Shenzhen 518060, *China*

(Received 3 April 2021; revised manuscript received 4 June 2021; accepted manuscript online 7 July 2021)

We develop a highly efficient scheme for numerically solving the three-dimensional time-dependent Schrödinger equation of the single-active-electron atom in the field of laser pulses by combining smooth exterior complex scaling (SECS) absorbing method and Arnoldi propagation method. Such combination has not been reported in the literature. The proposed scheme is particularly useful in the applications involving long-time wave propagation. The SECS is a wonderful absorber, but its application results in a non-Hermitian Hamiltonian, invalidating propagators utilizing the Hermitian symmetry of the Hamiltonian. We demonstrate that the routine Arnoldi propagator can be modified to treat the non-Hermitian Hamiltonian. The efficiency of the proposed scheme is checked by tracking the time-dependent electron wave packet in the case of both weak extreme ultraviolet (XUV) and strong infrared (IR) laser pulses. Both perfect absorption and stable propagation are observed.

Keywords: time-dependent Schrödinger equation (TDSE), smooth exterior complex scaling (SECS) absorbing method, Arnoldi propagator

PACS: 32.80.Fb, 33.20.Xx, 31.15.A– **DOI:** 10.1088/1674-1056/ac11d6

1. Introduction

In the study of ultrafast atom–laser interactions in modern strong-field physics and attosecond science, many simulations are based on the numerical solutions of the time-dependent Schrödinger equation (TDSE).[1–6] In cases where the laser pulses or the time-delays between the laser pulses are extremely long, the numerical TDSE calculation can be rather challenging. The methods to absorb the out-going electron wave packet are critical for the efficient simulations involving long-time propagation. The mask function[7,8] and the complex absorbing potential (CAP)[9–11] are two classes of widely applied absorbing methods. Such methods have the advantage of easy implementation, but they usually do not guarantee the complete absorption and sometimes the noise from the refection at the absorbing point can disturb the physical signal. On the other hand, the more complex absorbing methods with better absorption efficiency, such as the perfectly matched layer (PML) method[12–14] and the exterior complex scaling (ECS) method,[14–20] have also been applied in the numerical TDSE calculations.

The ECS method originates from the complex scaling (CS) method, in which the radial coordinate of the electron is scaled by a complex phase factor. In the early years, the CS method was applied to establish the analytic properties of the S-matrix in the complex momentum and energy planes[21,22] and to describe the resonance states.[23] In 1979, Simon[24] introduced the idea of ECS as an extension of the CS method. In the ECS method, the radial coordinate is kept real for small values, whereas for values larger than the absorbing point r_0, CS is performed. In this way, the energies of the bound states in the field-free atomic system are unchanged, but that of the continuum states are rotated downwards by an angle in the complex energy plane and the continuum wave functions are rendered square integrable. The application of ECS as an absorber for the out-going wave is built on a solid mathematics ground.[23–26] The extension of the ECS to numerical TDSE calculations was demonstrated by McCurdy *et al.*[27–29] Most authors took the sharp ECS method[14,16–20] and finite-element discrete variable representation (FE-DVR) in their TDSE calculations. The word "sharp" means that the scaling at r_0 is not continuous. In the FE-DVR frame, the discontinuity of the sharp ECS can be correctly handled as long as r_0 is taken to be the bridge point of two adjacent elements. In 2009, Tao *et al.*[19] reported a drawback of the ordinary ECS: the numerical error accumulates for long-time propagations and can only be controlled by extending the grid points. Recently, Scrinzi *et al.*[14,16,30] developed the infinite range exterior complex scaling (irECS) which promises to overcome such drawbacks.

In the early applications of the CS method in time-independent calculations, the Arnoldi (Lanczos) method was often used to calculate part of the eigenvalues of the corresponding non-Hermitian Hamiltonian.[31–33] The Arnoldi method was developed to be an efficient propagator in the time-dependent calculations by Park and Light in 1986.[34] Now Arnoldi propagator is popular in the simulations of high-dimensional systems such as two-electron atoms[4,35–38] and two-electron molecule H_2.[39,40] However, in a recent calcula-

†Corresponding author. E-mail: jiang.wei.chao@szu.edu.cn

© 2022 Chinese Physical Society and IOP Publishing Ltd

tion of double ionization of helium[41] by IR laser pulse using irECS method, a pessimistic judgement on the efficiency of Arnoldi propagator was made and Arnoldi propagator was finally given up in their study. In our recent work,[42] we showed that the Arnoldi propagator can be used for the strong IR laser pulses after proper modifications. In this paper, we will show that the Arnoldi propagator can be combined with the ECS method after additional modifications. We choose the smooth exterior complex scaling (SECS), instead of the sharp ECS, as the absorber. SECS has previously been developed in the time-independent calculations of the resonance states.[43,44] In comparison with the sharp ECS, we do not need to be worried about the discontinuity at the CS point r_0 and the limitation that r_0 must be a bridge point of two elements is not necessary in the SECS method. The application of sharp or smooth ECS leads to a non-Hermitian Hamiltonian matrix, whose eigenstates are not orthogonal as the usual inner product. Thus, the usual application of Arnoldi (or Lancozos) propagator for Hamiltonian matrix with Hermitian symmetry should be modified properly to take account of the general non-Hermitian symmetry. We report the modifications to these numerical methods and test them in the three-dimensional TDSE of single-active-electron (SAE) atom. We demonstrate that SECS can be a wonderful absorber by tracking the propagation of the electron wave packet. Meanwhile, the developed Arnoldi propagator for non-Hermitian Hamiltonian is quite stable and efficient even if strong IR laser pulse is used. Classical quiver motion of the freed electron in the strong IR laser pulse is clearly identified from the time-dependent radial distributions of the freed electron. To our knowledge, the successful combination of ECS and Arnoldi propagator for solving the TDSE has never been reported before.

Unless stated, we will adopt atomic units in this paper.

2. Theory

2.1. Time-dependent Schrödinger equation

The TDSE of the three-dimensional SAE atom is given by

$$\mathrm{i}\frac{\partial}{\partial t}\Psi(\boldsymbol{r},t) = H\Psi(\boldsymbol{r},t), \tag{1}$$

$$H = -\frac{1}{2}\nabla^2 + V(r) + H^{\mathrm{I}}(t), \tag{2}$$

where the Hamiltonian H consists of three parts, i.e., the kinetic energy $-(1/2)\nabla^2$, the electron–nucleus interaction potential $V(r)$ and the electron–laser interaction $H^{\mathrm{I}}(t)$. In the following, we take the atomic hydrogen as a test, for which the nuclear attractive potential $V(r)$ is explicitly expressed as

$$V(r) = -\frac{1}{r}. \tag{3}$$

The time-dependent electron–laser interaction Hamiltonian is given by

$$H^{\mathrm{I}}(t) = -\mathrm{i}\boldsymbol{A}(t)\cdot\nabla \tag{4}$$

in the velocity gauge.

The wave function $\Psi(\boldsymbol{r},t)$ is expanded in terms of spherical harmonics $|lm\rangle$

$$\Psi(\boldsymbol{r},t) = \sum_{l,m}\frac{R_{lm}(r,t)}{r}|lm\rangle. \tag{5}$$

Inserting Eq. (5) into Eq. (1) and performing some algebraic operations, we obtain the following equation for the radial wave functions $R_{lm}(r,t)$:

$$\begin{aligned}&\mathrm{i}\frac{\partial}{\partial t}R_{lm}(r,t)\\ &= \sum_{l'm'}\left[-\frac{1}{2}\frac{\partial^2}{\partial r^2} + \frac{l(l+1)}{2r^2} - \frac{1}{r} + H^{\mathrm{I}}{}_{lm,l'm'}\right]R_{l'm'}(r,t),\end{aligned} \tag{6}$$

where

$$\begin{aligned}H^{\mathrm{I}}{}_{lm,l'm'} &= -\mathrm{i}A(t)\left[\frac{\partial}{\partial r} + \frac{-l}{r}\right]a_{l-1,m}\delta_{l-1,l'}\delta_{m,m'}\\ &\quad -\mathrm{i}A(t)\left[\frac{\partial}{\partial r} + \frac{(l+1)}{r}\right]a_{l,m}\delta_{l+1,l'}\delta_{l+1,l'}\delta_{m,m'},\end{aligned} \tag{7}$$

with $a_{l,m}$ given by

$$a_{l,m} = \sqrt{\frac{(l+1)^2 - m^2}{(2l+1)(2l+3)}}. \tag{8}$$

2.2. Smooth exterior complex scaling

The SECS method is applied to scale the radial wave functions in Eq. (6). We map the real radial coordinate r to the complex variable u according to[44]

$$u = r + (\mathrm{e}^{\mathrm{i}\eta} - 1)\left[r + \frac{1}{2a}\ln\left(\frac{\cosh[a(r-r_0)]}{\cosh[a(r+r_0)]}\right)\right], \tag{9}$$

where a is the smooth parameter, r_0 is the critical point where the CS is performed and η is the angle that the real radial coordinate r is rotated into the upper complex plane. For $r_0 = 0$ or $a = 0$, the mapping is reduced to $u = r\mathrm{e}^{\mathrm{i}\eta}$, which is exactly the traditional CS method. As $a \to \infty$, the SECS in Eq. (9) is reduced to the sharp ECS,[14,16–20]

$$u = \begin{cases} r, & \text{if } r \le r_0,\\ r_0 + \mathrm{e}^{\mathrm{i}\eta}(r - r_0), & \text{if } r > r_0.\end{cases} \tag{10}$$

In the numerical implementation, however, the smooth parameter a cannot be too large in case the overflow takes place for the term $\cosh[a(r+r_0)]$ or $\cosh[a(r-r_0)]$. One example of SECS is provided in Fig. 1. The complex coordinate u as a function of the real radial coordinate r is shown in Fig. 1(a), and its derivative with respect to r is shown in Fig. 1(b).

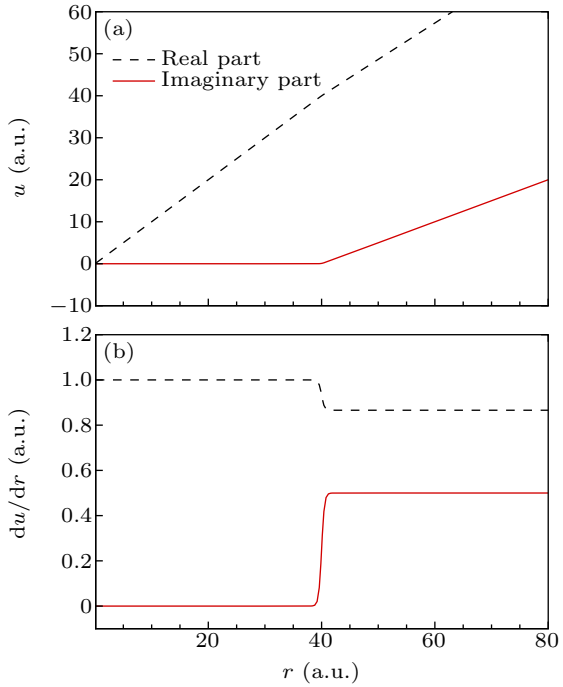


Fig. 1. (a) The complex coordinate u and (b) its first derivative $\mathrm{d}u/\mathrm{d}r$ as a function of the real radial coordinate r in the SECS [Eq. (9)]. The CS point r_0 is 40 a.u., the CS angle η is $\pi/6$, and the parameter a is 2.0 a.u.

The radial wave functions $R_{lm}(r,t)$ are analytically extended into the complex u plane $R_{lm}(r,t) \to R_{lm}[u(r),t]$. In order to simplify the expression of the volume element $\mathrm{d}u$ to be equal to $\mathrm{d}r$, the following new radial wave functions are defined:

$$\mathcal{R}_{lm}(r,t) = \left(\frac{\mathrm{d}u}{\mathrm{d}r}\right)^{\frac{1}{2}} R_{lm}[u(r),t]. \tag{11}$$

Replacing the variable r in Eq. 6 with u and then inserting $R_{lm}[u(r),t] = (\mathrm{d}u/\mathrm{d}r)^{-1/2}\mathcal{R}_{lm}(r,t)$ into Eq. 6, we obtain the following differential equations:

$$\mathrm{i}\frac{\partial}{\partial t}\mathcal{R}_{lm}(r,t) = \sum_{l'm'}\left[-\frac{1}{2}M + N + Q^{\mathrm{I}}{}_{lm,l'm'}\right]\mathcal{R}_{l'm'}(r,t), \tag{12}$$

where the operators M, N, and $Q^{\mathrm{I}}{}_{lm,l'm'}$ are expressed as

$$M = \left(\frac{\mathrm{d}u}{\mathrm{d}r}\right)^{-1}\frac{\partial^2}{\partial r^2}\left(\frac{\mathrm{d}u}{\mathrm{d}r}\right)^{-1}, \tag{13}$$

$$N = \frac{l(l+1)}{2u^2} - \frac{1}{u} - \frac{2\dfrac{\mathrm{d}^3u}{\mathrm{d}r^3}\dfrac{\mathrm{d}u}{\mathrm{d}r} - 3\left(\dfrac{\mathrm{d}^2u}{\mathrm{d}r^2}\right)^2}{8\left(\dfrac{\mathrm{d}u}{\mathrm{d}r}\right)^4}, \tag{14}$$

$$\begin{aligned} Q^{\mathrm{I}}{}_{lm,l'm'} = {} & -\mathrm{i}A(t)\left[\left(\frac{\mathrm{d}u}{\mathrm{d}r}\right)^{-\frac{1}{2}}\frac{\partial}{\partial r}\left(\frac{\mathrm{d}u}{\mathrm{d}r}\right)^{-\frac{1}{2}} + \frac{-l}{u}\right] \\ & \times a_{l-1,m}\delta_{l-1,l'}\delta_{m,m'} \\ & -\mathrm{i}A(t)\left[\left(\frac{\mathrm{d}u}{\mathrm{d}r}\right)^{-\frac{1}{2}}\frac{\partial}{\partial r}\left(\frac{\mathrm{d}u}{\mathrm{d}r}\right)^{-\frac{1}{2}} + \frac{(l+1)}{u}\right] \\ & \times a_{l,m}\delta_{l+1,l'}\delta_{l+1,l'}\delta_{m,m'}. \end{aligned} \tag{15}$$

Derivatives of u with respect to r can be explicitly expressed as[44]

$$\begin{aligned} \frac{\mathrm{d}u}{\mathrm{d}r} = {} & 1 + \frac{1}{2}(\mathrm{e}^{\mathrm{i}\eta} - 1) \\ & \times \{2 + \tanh[a(r-r_0)] - \tanh[a(r+r_0)]\}, \end{aligned} \tag{16}$$

$$\begin{aligned} \frac{\mathrm{d}^2u}{\mathrm{d}r^2} = {} & \frac{1}{2}a(\mathrm{e}^{\mathrm{i}\eta} - 1) \\ & \times \left\{\tanh^2[a(r+r_0)] - \tanh^2[a(r-r_0)]\right\}, \end{aligned} \tag{17}$$

$$\begin{aligned} \frac{\mathrm{d}^3u}{\mathrm{d}r^3} = {} & a^2(\mathrm{e}^{\mathrm{i}\eta} - 1)\Big\{\tanh[a(r+r_0)]\left\{1 - \tanh^2[a(r+r_0)]\right\} \\ & - \tanh[a(r-r_0)]\left\{1 - \tanh^2[a(r-r_0)]\right\}\Big\}. \end{aligned} \tag{18}$$

In numerical implementation, the radial functions $\mathcal{R}_{lm}(r,t)$ are further expanded in terms of the FE-DVR basis functions.[45] After applying SECS, the Hamiltonian matrix H is scaled to be a complex symmetric matrix.

2.3. Non-Hermitian Arnoldi propagator

In this subsection, we present the non-Hermitian Arnoldi propagation algorithm to solve the differential Eq. (12), which is still identical to the general form of TDSE [Eq. (1)], except for that the Hamiltonian matrix H is not Hermitian any more. The goal is to obtain the wave function $\Psi(t+\Delta t)$ in the next small time step when the wave function $\Psi(t)$ at moment t is known, i.e.,

$$\Psi(t+\Delta t) = U(t,t+\Delta t)\Psi(t), \tag{19}$$

where the evolution operator is formally expressed, for small time step Δt, as

$$U(t,t+\Delta t) = \mathrm{e}^{-\mathrm{i}H(t)\Delta t}. \tag{20}$$

The above short-time propagation can be approximately calculated in the Krylov subspace, which is constructed by repeatedly applying the Hamiltonian to the wave functions,

$$K_{N+1} = \left\{|\Psi(t)\rangle, H|\Psi(t)\rangle, H^2|\Psi(t)\rangle, \ldots, H^N|\Psi(t)\rangle\right\}, \tag{21}$$

where N is the order of the Krylov subspace, and it is typically around 10 in our calculations. Applying the Gram–Schmidt orthogonalization procedure, one can obtain the orthonormal basis vectors

$$Q_{N+1} = \{|q_0\rangle, |q_1\rangle, |q_2\rangle, \ldots, |q_N\rangle\}, \tag{22}$$

where

$$|q_0\rangle = \frac{1}{p_0}|\Psi(t)\rangle, \tag{23}$$

$$p_0 = \langle\Psi(t)|\Psi(t)\rangle. \tag{24}$$

The Arnold algorithm differs from the Lanczos algorithm in the way to obtain orthonormal basis vectors $|q_i\rangle$ and the corresponding matrix elements of the Hamiltonian. The Lanczos

algorithm is based on the fact that the Hermitian matrix in the Krylov subspace is tridiagonal. In this paper, we choose the more general Arnold algorithm[46] to treat the non-Hermitian Hamiltonian matrix. Though the scaled Hamiltonian matrix H is complex symmetric in the full FE-DVR space, such symmetry is not kept in the representation of Krylov subspace. The application of the Arnold algorithm results in a complex upper-Hessenberg Hamiltonian matrix,

$$h_{ij} = \left\langle q_i \middle| H \middle| q_j \right\rangle. \tag{25}$$

The upper-Hessenberg Hamiltonian matrix h is a small-size matrix whose diagonalization can be performed efficiently. We denote the eigenvalues and the eigenstates of the matrix h as h_i and $|Z_i\rangle$, respectively. The initial wave function $|q_0\rangle$ is expanded in terms of the eigenstates $|Z_i\rangle$,

$$|q_0\rangle = \sum_{i=0}^{N} a_i |Z_i\rangle . \tag{26}$$

The expansion coefficients a_i can be expressed as

$$a_i = \sum_{j=0}^{N} \left[A^{-1}\right]_{ij} \langle Z_j | q_0 \rangle , \tag{27}$$

where A is the overlap matrix of states $|Z_i\rangle$,

$$A_{ji} = \langle Z_j | Z_i \rangle , \tag{28}$$

and A^{-1} denotes the inverse matrix of A. We would like to stress that the matrix inversion in the numerical implementation is not necessary if the Hamiltonian is Hermitian, since A can be simplified to a unit matrix in that case. The fact that A is not a unit matrix is one important difference between the present propagator for general non-Hermitian matrix and the pervious propagator for Hermitian matrix.

Now we can approximate the short-time propagation Eq. (19) in the Krylov subspace as

$$|\Psi(t+\Delta t)\rangle = p_0 \sum_{k=0}^{N} a_k \exp\left(-\mathrm{i} h_k \Delta t\right) |Z_k\rangle , \tag{29}$$

where p_0 is defined in Eq. (24). When $\max[\mathrm{real}(h_k)]$ is large, one can split the centrifugal potential from the whole Hamiltonian to reduce $\max[\mathrm{real}(\mathrm{h_k})]$, as reported in our recent publication.[42] In the rest of the paper, if not stated otherwise, the whole radial box is discretized uniformly, each finite element having a size of 2 a.u. and being represented by 8 basis functions.

3. Tests for XUV laser pulse

In this section, we mainly test the applications to simple weak XUV laser pulse, where the electron dynamics can be simply predicted by the first-order perturbation theory. We adopt an XUV laser pulse with peak intensity 10^{12} W/cm^2, photon energy $\omega = 53.6$ eV (which is much larger than the ionization potential of atomic hydrogen, $I_\mathrm{p} = 13.6$ eV), and total duration of 10 optical cycles. The bound electron is freed by absorbing one photon, leaving the nucleus with kinetic energy of 40 eV or momentum of 1.7 a.u. To study the behavior of the out-going electron wave packet when it approaches the CS point r_0, we analyze the following angular-integrated time-dependent radial distributions after subtracting the component of the ground-state from the whole wave function:

$$D(r,t) = \int\int |\Psi(\boldsymbol{r},t)|^2 r^2 \sin\theta \,\mathrm{d}\theta \,\mathrm{d}\phi . \tag{30}$$

The time-dependent radial distribution $D(r,t)$ is shown in Fig. 2. In the first and the second rows in Fig. 2, one can clearly see that the freed electron packet moves to larger radius as the time increases. The slope of the peak signal is exactly the photoelectron momentum (1.7 a.u.). In all the panels applying SECS in Fig. 2, the CS point r_0 is fixed at 40 a.u. In the first row in Fig. 2, we check the influence of the width of the CS layer, r_c, on the absorption efficiency. The width is given by $r_\mathrm{c} = r_\mathrm{max} - r_0$, where r_max is the full size of the radial box. The results for two different r_c are shown in Figs. 2(a1) and 2(a2). As a comparison, the benchmark full result, where no SECS is applied and r_max is large enough, is shown in Fig. 2(a3). One can see that for the present simple one-photon ionization, the width $r_\mathrm{c} = 5$ a.u. is large enough to guarantee the perfect absorption [Fig. 2(a2)]. In Fig. 2(a2), it is clear that the electron signal quickly decays after the electron passes through the critical scaling point r_0, and no disturbance exists for radius smaller than r_0 in comparison with the benchmark full result shown in Fig. 2(a3). On the other hand, obvious reflection can be identified if r_c is extremely small (1 a.u.) as shown in Fig. 2(a1). More strict comparisons between the results of SECS with different r_c and benchmark "full" result are given in Fig. 2(c1), where the cut lines of $D(r,t)$ at $t = 38$ a.u. are shown. The SECS result for $r_\mathrm{c} = 5$ a.u. agrees with the benchmark full result perfectly for $r < r_0$, while the SECS result quickly decays for $r > r_0$.

In the second row in Fig. 2, we check the influence of the scaling angle η, which appears in Eqs. (9) and (10). η should be chosen in the range $[0, \pi/4]$. Taking $\eta = 0$ is identical to canceling the SECS absorber. Three different values of η are chosen in the second row in Fig. 2. One can find that the absorption efficiency is not sensitive to the choice of η as long as the CS layer is wide enough. In Fig. 2(c2), the cut lines of $D(r,t)$ at $t = 38$ a.u. are shown for different η. These cut lines agree with each other perfectly for $r < r_0$, and the values of $D(r,t)$ decay for $r > r_0$. As expected, the value of η has an influence on the decay rate, i.e., the larger η corresponds to the faster decay.

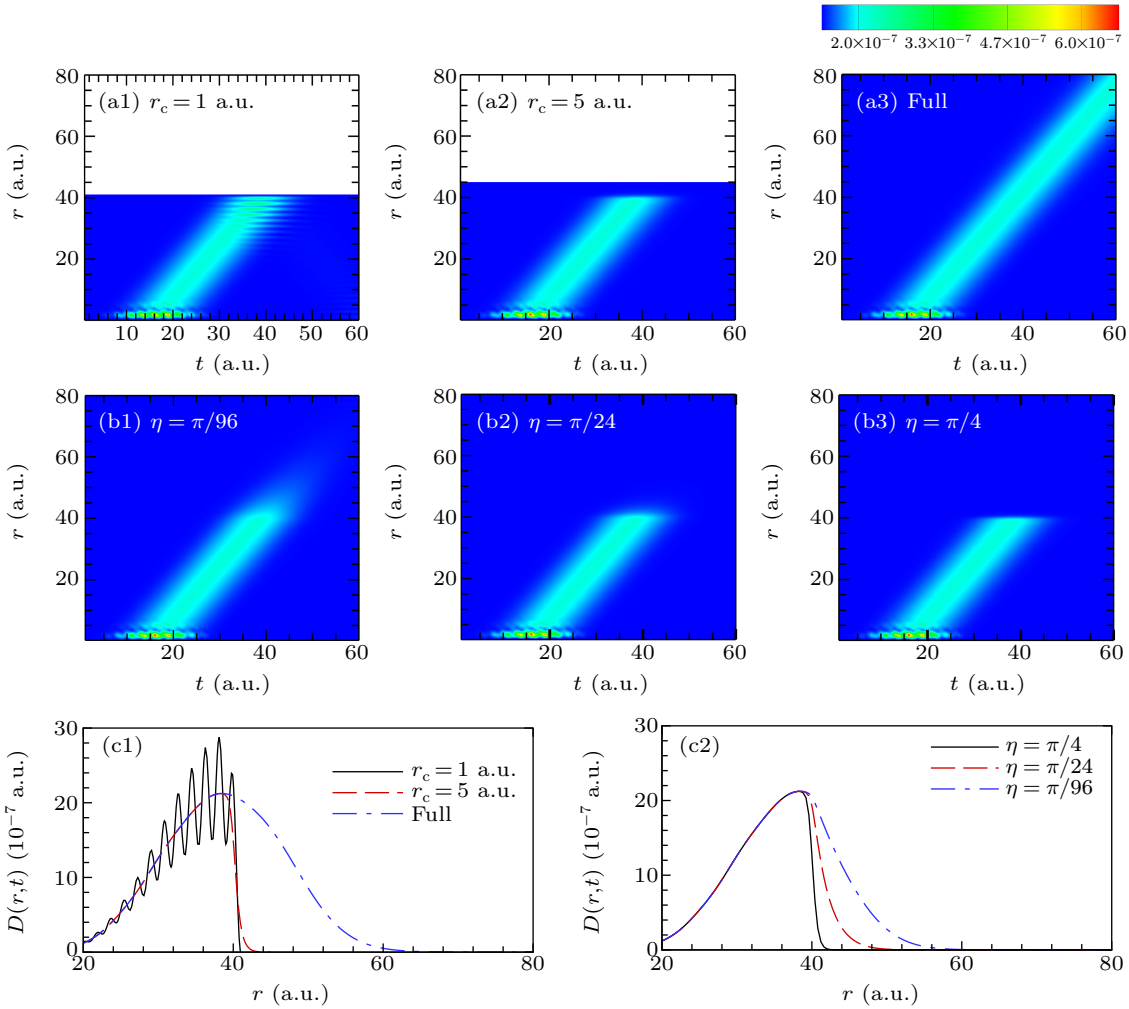


Fig. 2. The angular-integrated time-dependent radial probability density $D(r,t)$ [Eq. (30)] for different (a) widths r_c of the CS layer and (b) CS angles η in one-photon ionization of atomic hydrogen by weak XUV laser pulse at photon energy of 53.6 eV. In all SECS calculations, the CS point r_0 is fixed to be 40 a.u. In (a), $\eta = \pi/6$ is taken. In (b), $r_c = 40$ a.u. is taken. The cut lines of $D(r,t)$ at $t = 38$ a.u. are shown in (c). The contribution of the ground state has been subtracted from the whole wave function.

4. Tests for strong IR laser pulse

The TDSE calculation for the strong IR laser pulses is much more challenging than that for the XUV laser pulses. The amplitude α_0 of the classical quiver motion of the free electron in the monochromatic laser field can be rather large in the strong IR laser pulse. The freed electron can be driven back by the external strong IR field. One problem we would like to explore here is whether the value of the scaling point r_0 can be significantly smaller than the amplitude α_0 of the quiver motion of the freed electron. The quiver amplitude α_0 is given by

$$\alpha_0 = A_0/\omega, \tag{31}$$

where A_0 and ω are the amplitude of the vector potential and the central frequency of the laser pulse, respectively. In the following tests, we take the laser pulse with peak intensity of 1×10^{15} W/cm^2 and wavelength of 780 nm, and the quiver amplitude α_0 is evaluated to be 49.5 a.u.

To trace the quiver motion of the freed electron in the field of the strong IR laser pulse, the angular-integrated radial distribution $D(r,t)$ defined in Eq. (30) is not a good physical quantity since the quiver motion of electron is angularly distinguished. Therefore, we directly study the time-dependent probability density along the laser polarization direction, which is defined by

$$P(z,t) = r^2 \left|\psi(x=0, y=0, z, t)\right|^2. \tag{32}$$

Similar to Eq. (30), the component of the ground state has been subtracted from the whole wave function.

The time-dependent electron distribution $P(z,t)$ is shown in Fig. 3. In Figs. 3(a) and 3(b), the SECS result with $r_0 = 200$ a.u. and the benchmark full result are shown, respectively. The quiver motion of the freed electron in the external strong IR laser field can be identified clearly and the peak signal of the probability density precisely mimics the time-dependent electric field of the IR laser pulse. Different from the purely outgoing electron motion in the field of XUV laser pulse as shown in Fig. 2, the electron in the field of strong IR laser pulse

can be driven back towards the nucleus. In opposite to the outgoing electron wave packet, the in-coming electron wave does not decay in the complex layer.

We have calculated electron distributions $P(z,t)$ with various absorbing point r_0 but the same radial box size $r_{\max} = 260$ a.u., and the corresponding cut lines of the distribution $P(z,t)$ at $t = 201$ a.u. are shown in Fig. 3(c). As tested, the minimum width of the CS layer r_c required for convergence is about 80 and 10 a.u. for $r_0 = 80$ and 200 a.u., respectively. For r_0 smaller than $\alpha_0 = 49.5$ a.u., the total population of the electron in the whole space, i.e., $\langle\Psi(t)|\Psi(t)\rangle$, can grow from 1 to an extremely huge number and the numerical result completely makes no sense. In Fig. 3(c), we can see that the SECS result for $r_0 = 60$ a.u. does not produce correct result for $r < r_0$, while those results for $r_0 \geq 80$ a.u. agree with each other perfectly in the radial range $r < r_0$. Thus, the CS point r_0 in the SECS calculation should be at least larger than the quiver amplitude α_0. In fact, the value of r_0 may need to be further increased for longer laser pulse.[19]

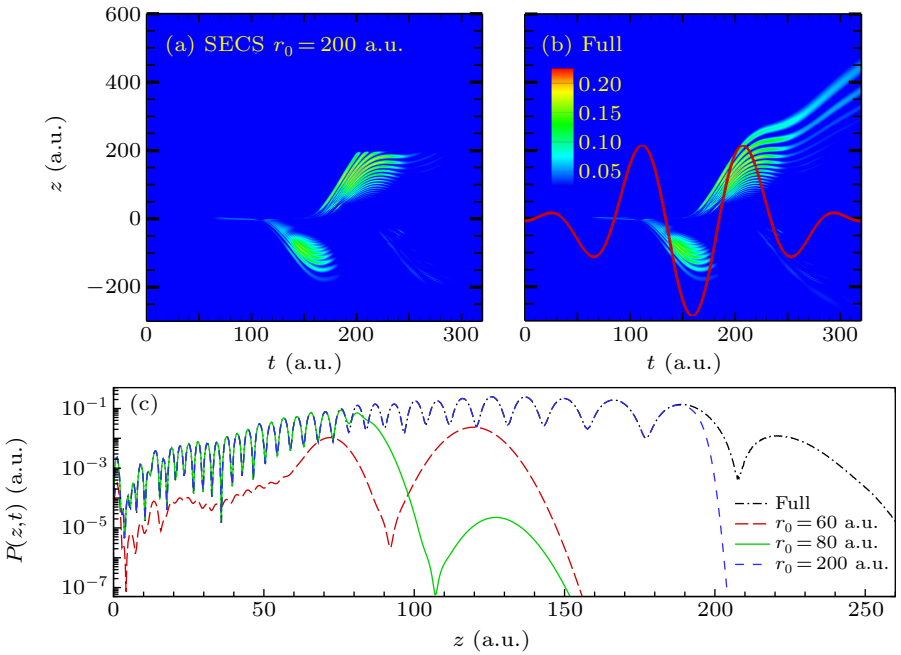


Fig. 3. The time-dependent angular-distinguished radial probability density $P(z,t)$ [Eq. (32)] from (a) SECS calculation with $r_0 = 200$ a.u., $r_{\max} = 260$ a.u. and (b) benchmark full TDSE results with enough large box for a $\sin^2$-shape IR laser pulse at wavelength of 780 nm, intensity of 1×10^{15} W/cm^2 and duration of 3 cycles. In (b), the time-dependent electron field of the IR laser pulse is also shown as a red solid line. The cut lines of $P(z,t)$ at $t = 201$ a.u. are shown in (c) for different CS points r_0 but the same radial box size $r_{\max} = 260$ a.u. Similar to Fig. 2, the contribution of the ground state has been subtracted from the whole wave function.

Here, we would like to provide a comparison of the SECS with another often-used absorber — the traditional wave-splitting absorber. In the latter scheme, at each time iteration, the electron wavefunction is multiplied by an absorbing function in the form of

$$f_a = \begin{cases} 1, & \text{if } r \leq r_0, \\ \exp\left[-4\left(\dfrac{r-r_0}{\sigma}\right)^2\right], & \text{if } r > r_0, \end{cases} \tag{33}$$

where the absorbing point is also denoted with r_0, and σ is a constant parameter the value of which should be properly chosen. By such multiplication, components of the high-energy electron in the wavefunction are smoothly discarded. Comparison of the angular-distinguished radial probability densities $P(z,t)$ at $t = 201$ a.u. obtained with the SECS and the wave-splitting absorber is shown in Fig. 4. r_0 and the radial box size $r_{\max}$ are kept the same for both absorbers. When $r_0 = 80$ a.u., $r_{\max}$ and σ are set to be 160 and 30 a.u., respectively. The result obtained with the wave-splitting absorber deviates substantially from the SECS result (which is convergent as examined). When r_0 is increased to 200 a.u., where $r_{\max}$ and σ are respectively set to be 210 and 3 a.u., results obtained using both absorbers coincides with each other. Apparently, the SECS has better absorbing ability than the wave-splitting absorber, since the former can realize perfect absorption even when r_0 is rather small. The present work is partly inspired by the paper on the irECS absorber.[16] In the irECS scheme, the CS layer contains only a small number of discretization points, yet perfect absorption is still realized. To examine whether the SECS absorber could use much coarser discretization in the CS layer, we recalculate the curve obtained using the SECS absorber in Fig. 4(a) with larger element size for $r > r_0$ while the element size for $r < r_0$ remains 2 a.u. and the number of basis functions used for any element in the whole space remains 8. We find that, for the curve to be converged, the maximum element size allowed is about 4 a.u. Reduction in computa-

tional cost by using larger element size for $r > r_0$ is limited. To reach the high efficiency of the irECS absorber by using very coarse discretization in our method, technical challenges remain to be overcome.

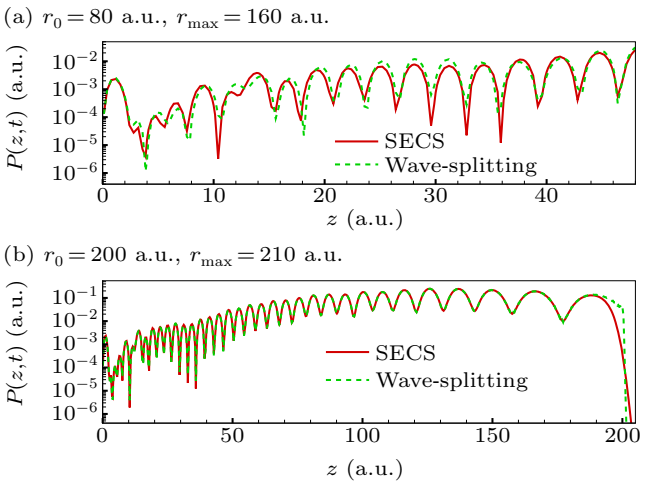


Fig. 4. Comparison of the angular-distinguished radial probability density $P(z,t)$ at $t = 201$ a.u. obtained using two different absorbers — the SECS and the wave-splitting absorber. (a) $r_0 = 80$ a.u., $r_{max} = 160$ a.u.; (b) $r_0 = 200$ a.u., $r_{max} = 210$ a.u. Laser parameters are the same as those in Fig. 3.

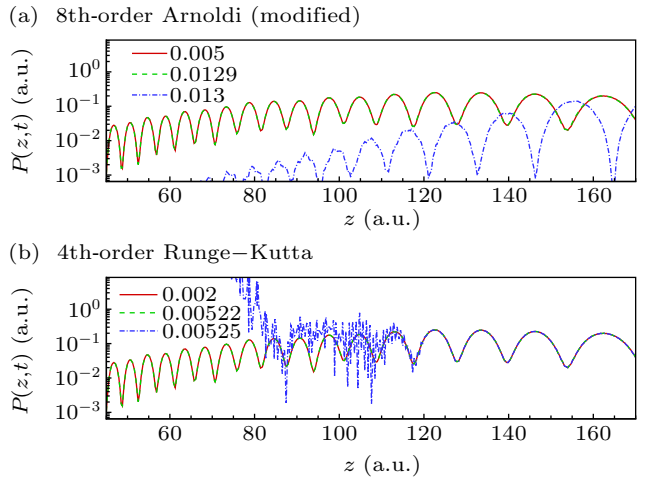


Fig. 5. Comparison of the angular-distinguished radial probability densities $P(z,t)$ at $t = 200$ a.u. for different time steps Δt obtained using the modified (non-Hermitian) Arnoldi propagator (a) and Runge–Kutta propagator (b). The radial box size is 260 a.u. and $r_0 = 200$ a.u. Laser parameters are the same as those in Fig. 3.

To demonstrate the propagation efficiency of the proposed non-Hermitian Arnoldi propagator, we test its maximum time step Δt required for convergence against that of the 4th-order Runge–Kutta propagator [Fig. 5]. In both cases, the SECS absorber is adopted for absorption, and the radial box size is chosen to be 260 a.u., and $r_0 = 200$ a.u. The order of the Arnoldi propagator is set to be 8, an often-used order. For both absorbers, the order equals to how many times the Hamiltonian is multiplied with the wavefunction, and these multiplications are the major computational cost. As can be seen in Fig. 5, for the non-Hermitian Arnoldi propagator the maximum Δt required is between 0.0129 a.u. and 0.013 a.u., while in the Runge–Kutta case the maximum Δt lies between 0.00522 a.u. and 0.00525 a.u. The maximum Δt allowed in the former case is approximately two times of that in the latter case. As a result, the two propagators have comparable efficiencies. Traditionally, the Arnoldi propagator has been considered more efficient than the Runge–Kutta one. However, in a recent work on double ionization by IR fields,[41] where the irECS was used as the absorber, the authors found that the Arnoldi propagator has no advantage in efficiency over the Runge–Kutta. Our work provides a similar observation. Finally, we would like to stress that, in all the calculations in this work, the centrifugal potential is split out from the whole Hamiltonian by using the scheme we proposed in Ref. [42], which greatly improves the efficiency of time propagation of the wavefunction. It is under this condition that our comparison of the two propagators is done.

5. Conclusions

In this work, we have successfully combined the SECS and non-Hermitian Arnoldi propagator to efficiently solve the three-dimensional TDSE of the SAE atom. The time-dependent angular-integrated and angular-distinguished radial distributions of the electron are calculated. From these distributions, the absorption of the out-going electron wave packet and the quiver motion of the freed electron in the field of strong IR laser can be clearly observed. We have shown that SECS can be a perfect absorption method as long as the CS radial coordinate r_0 and the width of the CS layer are properly chosen such that its absorbing ability surpassing that of the traditional wave-splitting absorber. When the strong IR laser pulses are used, one should be careful that the scaling coordinate r_0 should be significantly larger than the amplitude of the quiver motion of the freed electron. The non-Hermitian Arnoldi propagation method we developed is stable not only for weak XUV laser pulses but also for strong IR laser pulses. Its efficiency is found to be comparable to that of the Runge–Kutta propagator, supporting the discussions in Ref. [41]. The numerical scheme proposed in this work is particularly useful in simulations requiring long-time propagation. It may also be useful for more complex systems with electron correlations. At last, the modified Arnoldi propagator has the potential to be combined with the irECS absorbing method.

Acknowledgment

Project supported by the National Natural Science Foundation of China (Grant Nos. 12074265 and 11804233).

References

[1] Miyagi H and Madsen L B 2016 *Phys. Rev. A* **93** 033420

[2] Huismans Y, Rouzée A, Gijsbertsen A, Jungmann J H, Smolkowska A S, Logman P S W M, Lépine F, Cauchy C, Zamith S, Marchenko T, Bakker J M, Berden G, Redlich B, van der Meer A F G, Muller H G, Vermin W, Schafer K J, Spanner M, Ivanov M Y, Smirnova O, Bauer D, Popruzhenko S V and Vrakking M J J 2011 *Science* **331** 61

[3] Pazourek R, Feist J, Nagele S and Burgdörfer J 2012 *Phys. Rev. Lett.* **108** 163001

[4] Jiang W C, Shan J Y, Gong Q H and Peng L Y 2015 *Phys. Rev. Lett.* **115** 153002

[5] Pazourek R, Nagele S and Burgdörfer J 2015 *Rev. Mod. Phys.* **87** 765

[6] Peng L Y, Jiang W C, Geng J W, Xiong W H and Gong Q H 2015 *Phys. Rep.* **575** 1

[7] Krause J L, Schafer K J and Kulander K C 1992 *Phys. Rev. A* **45** 4998

[8] Tong X M, Hino K and Toshima N 2006 *Phys. Rev. A* **74** 031405

[9] Riss U V and Meyer H D 1995 *J. Phys. B* **28** 1475

[10] Riss U and Meyer H 1996 *J. Chem. Phys.* **105** 1409

[11] Santra R 2006 *Phys. Rev. A* **74** 034701

[12] Collino F 1997 *J. Comput. Phys.* **131** 164

[13] Nissen A, Karlsson H O and Kreiss G 2010 *J. Chem. Phys.* **133** 054306

[14] Scrinzi A, Stimming H and Mauser N 2014 *J. Comput. Phys.* **269** 98

[15] McCurdy C W, Baertschy M and Rescigno T N 2004 *J. Phys. B* **37** R137

[16] Scrinzi A 2010 *Phys. Rev. A* **81** 053845

[17] Orimo Y, Sato T, Scrinzi A and Ishikawa K L 2018 *Phys. Rev. A* **97** 023423

[18] He F, Ruiz C and Becker A 2007 *Phys. Rev. A* **75** 053407

[19] Tao L, Vanroose W, Reps B, Rescigno T N and McCurdy C W 2009 *Phys. Rev. A* **80** 063419

[20] Rescigno T N, Baertschy M, Byrum D and McCurdy C W 1997 *Phys. Rev. A* **55** 4253

[21] Regge T 1959 *Il Nuovo Cimento* **14** 951

[22] Regge T 1960 *Il Nuovo Cimento* **18** 947

[23] Balslev E and Combes J M 1971 *Commun. Math. Phys.* **22** 280

[24] Simon B 1979 *Phys. Lett. A* **71** 211

[25] Simon B 1972 *Commun. Math. Phys.* **27** 1

[26] Simon B 1973 *Ann. Math.* **97** 247

[27] McCurdy C W, Stroud C K and Wisinski M K 1991 *Phys. Rev. A* **43** 5980

[28] McCurdy C W and Stroud C K 1991 *Comput. Phys. Commun.* **63** 323

[29] McCurdy C W, Horner D A and Rescigno T N 2002 *Phys. Rev. A* **65** 042714

[30] Weinmüller M, Weinmüller M, Rohland J and Scrinzi A 2017 *J. Comput. Phys.* **333** 199

[31] Dallwig S, Fahrer N and Schlier C 1992 *Chem. Phys. Lett.* **191** 69

[32] Suno H, Andric L, Grozdanov T P and McCarroll R 2000 *Physics Letters A* **265** 377

[33] Milfeld K F and Moiseyev N 1986 *Chem. Phys. Lett.* **130** 145

[34] Park T J and Light J C 1986 *J. Chem. Phys.* **85** 5870

[35] Smyth E S, Parker J S and Taylor K 1998 *Comput. Phys. Commun.* **114** 1

[36] Parker J S, Doherty B J S, Taylor K T, Schultz K D, Blaga C I and DiMauro L F 2006 *Phys. Rev. Lett.* **96** 133001

[37] Feist J, Nagele S, Pazourek R, Persson E, Schneider B I, Collins L A and Burgdörfer J 2008 *Phys. Rev. A* **77** 043420

[38] Jiang W C, Xiong W H, Zhu T S, Peng L Y and Gong Q H 2014 *J. Phys. B* **47** 091001

[39] Guan X, Bartschat K and Schneider B I 2011 *Phys. Rev. A* **83** 043403

[40] Jiang W C, Peng L Y, Geng J W and Gong Q H 2013 *Phys. Rev. A* **88** 063408

[41] Zielinski A, Majety V P and Scrinzi A 2016 *Phys. Rev. A* **93** 023406

[42] Jiang W C and Tian X Q 2017 *Opt. Express* **25** 26832

[43] Karlsson H O 1998 *J. Chem. Phys.* **109** 9366

[44] Moiseyev N 1998 *J. Phys. B* **31** 1431

[45] Rescigno T N and McCurdy C W 2000 *Phys. Rev. A* **62** 032706

[46] Dundas D 2002 *Phys. Rev. A* **65** 023408